



HAL
open science

Unravelling the secrets of the resistance of GaN to strongly ionising radiation

Miguel Sequeira, Jean-Gabriel Mattei, Henrique Vazquez, Flyura Djurabekova, Kai Nordlund, Isabelle Monnet, Pablo Mota-Santiago, Patrick Kluth, Clara Grygiel, Shuo Zhang, et al.

► To cite this version:

Miguel Sequeira, Jean-Gabriel Mattei, Henrique Vazquez, Flyura Djurabekova, Kai Nordlund, et al.. Unravelling the secrets of the resistance of GaN to strongly ionising radiation. *Communications Physics*, 2021, 4, pp.51. 10.1038/s42005-021-00550-2. hal-03666342

HAL Id: hal-03666342

<https://hal.science/hal-03666342v1>

Submitted on 18 Sep 2024








HAL is a multi-disciplinary open access archive for the deposit and dissemination of scientific research documents, whether they are published or not. The documents may come from teaching and research institutions in France or abroad, or from public or private research centers.

L'archive ouverte pluridisciplinaire **HAL**, est destinée au dépôt et à la diffusion de documents scientifiques de niveau recherche, publiés ou non, émanant des établissements d'enseignement et de recherche français ou étrangers, des laboratoires publics ou privés.



Distributed under a Creative Commons Attribution 4.0 International License

Unravelling the secrets of the resistance of GaN to strongly ionising radiation

Miguel C. Sequeira ^{1✉}, Jean-Gabriel Mattei², Henrique Vazquez³, Flyura Djurabekova ³, Kai Nordlund ³, Isabelle Monnet ², Pablo Mota-Santiago⁴, Patrick Kluth ⁴, Clara Grygiel ², Shuo Zhang⁵, Eduardo Alves¹ & Katharina Lorenz ^{1,6}

GaN is the most promising upgrade to the traditional Si-based radiation-hard technologies. However, the underlying mechanisms driving its resistance are unclear, especially for strongly ionising radiation. Here, we use swift heavy ions to show that a strong recrystallisation effect induced by the ions is the key mechanism behind the observed resistance. We use atomistic simulations to examine and predict the damage evolution. These show that the recrystallisation lowers the expected damage levels significantly and has strong implications when studying high fluences for which numerous overlaps occur. Moreover, the simulations reveal structures such as point and extended defects, density gradients and voids with excellent agreement between simulation and experiment. We expect that the developed modelling scheme will contribute to improving the design and test of future radiation-resistant GaN-based devices.

¹IPFN, Instituto Superior Técnico, University of Lisbon, Lisbon, Portugal. ²CIMAP, Normandie University, CEA, CNRS, UNICAEN, ENSICAEN-BP5133, Caen Cedex 5, France. ³Department of Physics, University of Helsinki, Helsinki, Finland. ⁴Department of Electronic Materials Engineering, Research School of Physics, Australian National University, Canberra, ACT, Australia. ⁵School of Nuclear Science and Technology, Lanzhou University, Lanzhou, China. ⁶Instituto de Engenharia de Sistemas e Computadores – Microsistemas e Nanotecnologias (INESC MN), Lisbon, Portugal. ✉email: miguel.sequeira@tecnico.ulisboa.pt

Group III nitrides have been the semiconductors of choice for some of the most notable technological achievements of the last few decades. They have found application in devices such as light-emitting diodes, laser diodes and high-electron mobility transistors (HEMTs). More recently, they are raising the standards once again, this time in the field of radiation-hard electronics. For instance, when comparing GaN with Si-based HEMTs, the former not only offer higher efficiency, work at higher voltages and have faster-switching transitions but also enjoy better thermal stability and are more resistant to radiation^{1,2}. Space and high-energy physics are two examples of areas with ongoing intense research that could benefit enormously from these more efficient and enduring devices. The European Space Agency is currently employing a new generation of space communication systems based on GaN HEMTs in its Porba-V satellite, so far delivering greatly improved data transmission rates and working reliability³, as well as in its Biomass satellite due for launch in 2022⁴. The extreme radiation present in these environments introduces significant challenges that should be addressed in order to advance such technologies.

While the effect of low- to medium-energy ions in GaN is relatively well understood^{5–7}, the high-energy radiation regime is still under debate. In space, the latter is of special interest when studying the influence of the so-called HZE (high atomic number Z and high energy) ions, a crucial component of the galactic cosmic radiation (GCR) and solar radiation spectra. Although less abundant than proton and gamma radiation, HZE ions (such as Fe and Si) have a very high ionisation power and relatively high fluxes^{8–10}. This likely not only accelerates the degradation but also can cause single-event catastrophic failure of devices¹¹.

In this communication, we address fundamental aspects of the interaction of strongly ionising particles with GaN, namely its response to the so-called swift heavy ion (SHI) radiation. With typical energies in the MeV and above range per nucleon, SHIs lose their energy in the target primarily via electronic interactions. In semiconductors, this often induces ionisation spikes along their paths that promote the formation of latent tracks¹² and surface effects¹³. Moreover, it has been reported that SHI radiation can lead to the recovery of pre-damaged material^{14–18}, including the recrystallisation of amorphous materials.

Recently, conflicting reports have been published on the matter of strongly ionising radiation effects on GaN. Sall et al.¹⁹ used transmission electron microscopy (TEM) to study GaN films irradiated with SHI and concluded that those are capable of amorphising the crystal. This result opposes the one obtained

previously by Kucheyev et al.²⁰, who used Rutherford back-scattering spectrometry/channelling (RBS/C) to show that even when GaN films are irradiated with high fluences (above $1 \times 10^{12} \text{ cm}^{-2}$), they presented a defective but still crystalline structure. The situation becomes more surprising when we realise that Kucheyev et al. studied SHIs with higher energies than some studied by Sall et al. Moreover, Kucheyev et al. observe that their experimental data follow neither Poisson nor Gibbons models²¹, which already points to the existence of complex damage formation and annihilation mechanisms.

Here, we identify the processes leading to this apparent contradiction by applying a two-temperature model-molecular dynamics (TTM-MD) simulation scheme capable of reproducing the experimental results obtained with both techniques, TEM and RBS/C, and also by electron energy loss spectroscopy (EELS). The TTM is one of the most used approximations to describe the first femtoseconds of the SHI interaction with matter. Within this model, the ionisation spike is depicted as a hot electron gas of temperature T_e that quickly relaxes its energy into the target lattice via electron-phonon interactions²². However, the TTM does not take into consideration the structural dynamics of the crystal, hence hiding compelling phenomena such as phase transitions or defect dynamics. Thus, the TTM output (i.e., the energy profile of the lattice) is deposited into a MD cell. This simulation scheme, often referred to as TTM-MD, has found success in describing the interaction of SHIs with different materials (e.g.,^{17,18,23}). A detailed discussion on the implementation of the TTM for GaN is presented in the Methods section and Supplementary Note 1.

Results

Recrystallisation. We begin by studying 3- μm thick GaN films on a Al_2O_3 substrate irradiated with 185 MeV Au ions (with an electronic energy loss of $\epsilon_e = 33 \text{ keV/nm}$ as calculated using the SRIM code²⁴). The simulations describing this SHI show that the initial spike induces a solid-liquid phase transition in the crystal, forming a cylindrical track along the SHI path. The radius of this molten track increases radially, reaching its maximum value of $r_t = 4.4 \text{ nm}$, 13 ps after the SHI impact, as Fig. 1a shows. The high lattice temperature (up to 8000 K), along with the strong confinement of the molten track within the crystalline GaN matrix, gives rise to a high-pressure state. This opens the possibility for the track to recover via recrystallisation similar to what was shown experimentally by X-ray diffraction during the

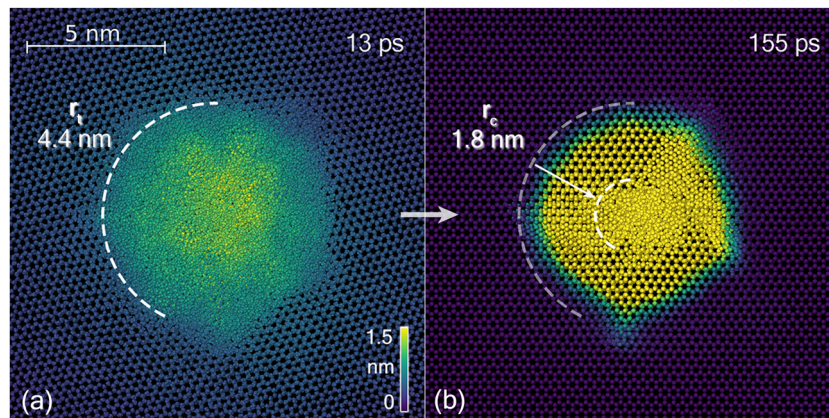


Fig. 1 Simulated 185 MeV Au ion track cross-sections in the deeper regions at different stages. **a** It shows the moment when the melted zone radius reaches its maximum value. **b** It shows the final state of the track, demonstrating the partial recrystallisation of the initial melted volume. The colour scheme represents the magnitude of the displacement of the atoms from their original positions. Refer to Supplementary Movie 1 to visualise the entire recrystallisation process.

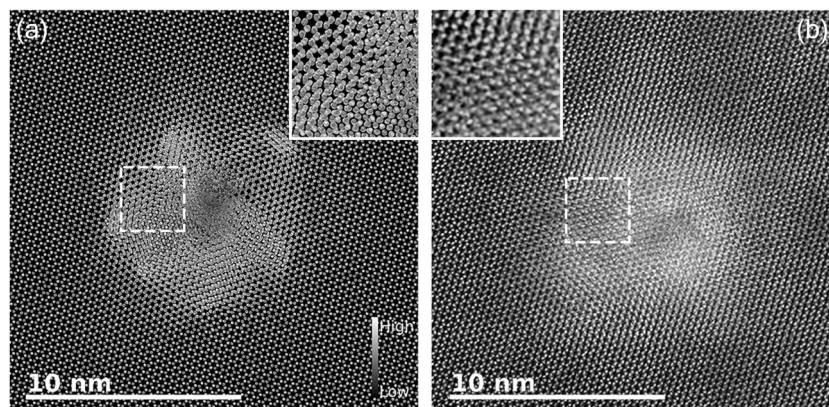


Fig. 2 Plan-view images of the final track of a 185 MeV Au ion in the deeper regions. **a** Simulated image. **b** Experimental transmission electron microscopy-high-angle annular dark-field image. The insets highlight the presence and similarities of the extended defects in both images.

cooling of high-pressure melted GaN²⁵. Indeed, at 13 ps, the recrystallisation starts at the edge of the track and proceeds inwards as the system cools down. Due to the high-pressure state, extended defects begin to form as well. When the crystal finally reaches room temperature, Fig. 1b, the morphology of the track consists of a damaged, yet highly crystalline, shell with an outer radius equal to r_t and a significantly smaller amorphous core with a radius $r_c = 1.8$ nm (see also Supplementary Movie 1 to visualise the entire recrystallisation process).

Simulated and experimental plan-view TEM in a high-angle annular dark-field setup (TEM-HAADF) images for 185 MeV Au ions are shown in Fig. 2a, b, respectively. We found an exceptional dimensional and morphological agreement. The predicted values for r_t and r_c , have a straightforward correspondence to the outer (less damaged) and the inner (more damaged) radii of the track seen in the experimental TEM-HAADF image. Moreover, the defects in the outer part of the track induce misoriented crystallographic domains in both simulated and experimental images, as evidenced in the magnifications in Fig. 2. This similarity suggests that the simulations reproduce the nature and influence of the extended defects accurately.

Defect formation. To further study the defects created, we apply the dislocation extraction algorithm (DXA)²⁶ to the simulation cell. As shown in Fig. 3a, the DXA reveals the existence of dislocation edges (green lines) and stacking faults (orange lines) in the recrystallised volume. Comparing the simulated and experimental cross-sectional TEM-HAADF images, Fig. 3a, b, respectively, reveals a striking resemblance between them.

In addition, the incorporation of atoms into the extended defects leads to a distinct density profile, as the overlay in Fig. 3a, b shows. The ion track morphology consists of a low-density core surrounded by a high-density shell. Using EELS, we found the predicted density profile to be in excellent agreement with the experimental one, Fig. 3c. Moreover, the obtained density of the amorphous core in the simulations is of 5.1 g/cm³, comparable with that of amorphous GaN predicted by density functional theory²⁷. These results strengthen the validity of the predicted dynamics, namely the recrystallisation and the formation of extended defects.

We suggest that the formation of the extended defects and concomitant density gradient is likely responsible for interrupting recrystallisation. After some time, the density in the melted volume reaches a critical point where recrystallisation becomes inviable.

Surface effects. Near the surface, there is an important additional mechanism of pressure relaxation. While in the deeper

regions, the pressure within the track can only relax radially, near the surface, it can relax upwards as well. This difference creates a pressure gradient along the SHI path that ultimately leads to the sputtering of a considerable amount of Ga and N atoms. Consequently, as shown in Fig. 4a, near the surface, we found not only voids within the track but also a hillock on the top of it. Despite the sputtering, a considerable amount of recrystallisation still occurs, particularly in the deeper regions of the cell. Comparing the simulated and experimental cross-sectional TEM-HAADF images, Fig. 4b, c, respectively, an excellent agreement is found. Not only the presence of very low-density pockets, presumably voids, inside a highly damaged track is evident in the experiment, but also their shape, density and distribution are simulated accurately. The largest low-density pocket observed in the experimental image (Fig. 4c) has a lateral dimension of approximately 4 nm, comparable with the predicted one of about 3.6 nm (Fig. 4a, b). Moreover, the voids are elongated along the track direction in both experimental and simulated images. Regarding their density inside the track, we obtain the experimental value of approximately 0.30–0.35 voids/nm, neighbouring the 0.35 voids/nm obtained from the simulations near the surface.

Note that the differences observed in the surface and bulk simulations are solely due to surface effects. The energy loss is assumed to be equal in both simulations, a fair assumption since the thickness of the GaN films is considerably smaller than the range of the SHIs.

Recrystallisation upon overlapping impacts. Remarkably, efficient recrystallisation also occurs when a SHI impacts pre-damaged material. This has substantial implications in the damage evolution with fluence. As shown in Fig. 5, the amorphous core of an ion track is almost entirely recrystallised upon the overlapping impact of a second SHI. Interestingly, this phenomenon occurs even when the track overlap is not direct, i.e., when the amorphous track core from the first SHI is slightly outside of the melted volume induced by the second SHI. This implies that the recrystallisation cross-section, with radius r_r , is greater than the initial melting cross-section ($r_t = 4.4$ nm). By performing simulations for tracks at different distances, we estimate r_r to be approximately 6.5 nm. Despite this recovery being substantial for direct and indirect overlaps, the formation of extended defects is enhanced in the latter case.

Surprisingly, even the voids seen in the surface simulation are partially recovered when overlapped by another SHI. This recovery is more efficient in the deeper regions leading to a density gradient of voids with depth.

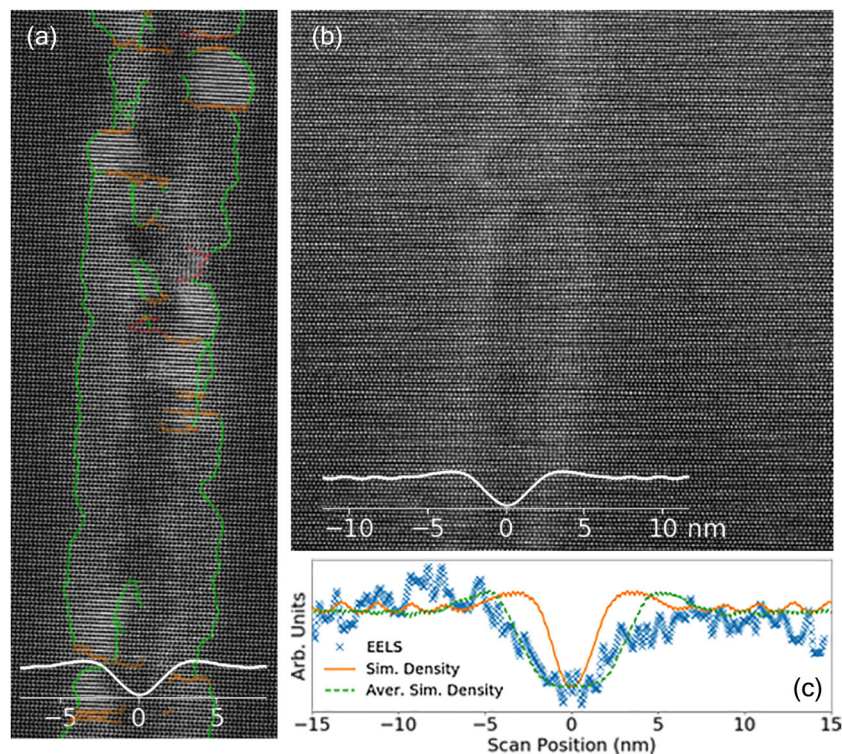


Fig. 3 Cross-sectional images of the final state of the 185 MeV Au ion track in the deeper regions. **a** Simulated track with the green and orange lines representing the dislocation edges and stacking faults, respectively, as obtained from the dislocation extraction algorithm analysis. **b** Experimental cross-sectional transmission electron microscopy-high-angle annular dark-field image. **c** Simulated and experimental density profiles (also overlaid in **(a)** and **(b)**). The dashed line corresponds to the average of the simulated profile over a window of multiple slices, as a means to introduce the experimental resolution (see Methods).

Damage evolution. The pronounced lattice recovery within a single track and upon multiple impacts makes it unlikely for the crystal to become fully amorphised, even for high fluences. In Fig. 6a, we present the RBS/C measurements of samples irradiated with different fluences of 185 MeV Au ions. As expected, the backscattering yield in the aligned spectra increases with the ion fluence as the defect concentration rises. Nonetheless, even for the highest fluence of $1 \times 10^{13} \text{ cm}^{-2}$, the backscattering yield stays well below the random level revealing that the single-crystalline nature of the sample is preserved. For this fluence, Poisson statistics indicate that the whole sample has suffered a high number of impact overlaps. This resistance to radiation follows the results of Kucheyev et al.²⁰ suggesting that for 200 MeV Au irradiation, no amorphisation of GaN occurs even for high fluences.

To further interpret the RBS/C results, it is paramount to take into consideration the full description of the track morphology, in particular, the presence of extended defects, surface voids and density gradients. None of these structures is considered by prevalent RBS/C models, such as the two-beam approximation²⁸ or the master equation approach²⁹, despite impacting the measurements significantly. Extended defects, in particular, are a well-known issue in RBS/C analysis due to the enhanced dechannelling effect they create⁶. If not taken into account, the models often result in inaccurate damage-depth profiles³⁰.

Regarding the influence of density gradients and voids in RBS/C, to the best of our knowledge, they have not yet been studied. To address these issues, we apply the RBSADEC code³¹, a Monte Carlo implementation of a binary collision algorithm, that replicates the RBS/C experiment in cells with atoms in arbitrary positions. Thus, it is suitable to predict the RBS/C spectra from the final state of our MD simulations, taking into account all the morphological features of the track inherently. A realistic cell for

the RBSADEC simulations is created by repeating and joining the final cells of the MD surface and bulk simulations. To account for overlap effects, for each fluence, we determine the appropriate lateral size and the number of impacts inside the MD cell using Poisson statistics. The distance between impacts, an essential parameter due to the recrystallisation dynamics, is chosen based on numerical calculations. Refer to Methods section and Supplementary Note 2 for further details on the implementation of the RBSADEC code.

Figure 6 shows an excellent agreement between simulated and experimental RBS/C spectra. Comparison with simulations using only the bulk MD cell reveals that surface voids lower the backscattering yield of the aligned spectrum, as observed in the RBS/C spectra shown in Fig. 6 for the first 300 nm (i.e., energies above 1350 keV). Furthermore, we note that the density of voids is not constant with depth and depends on the fluence. Although all the impacts induce voids until approximately the same depth (approximately 320 nm in the case of the 185 MeV Au ion), the deeper voids formed by previous impacts are recovered in the event of an overlap. Therefore, the areas with more overlaps (e.g., two impacts) have a smaller fraction of deep-voids than those with fewer overlaps (e.g., one impact). As the number of overlaps increases, this effect becomes more pronounced and leads to an inhomogeneous depth distribution of voids, which has a significant influence on the aligned spectra.

Note that there is no fitting involved except for the mentioned surface effects. The RBS/C spectra beyond 320-nm depth are directly simulated from the untreated bulk MD cell. In line with the TEM results, the spectra strongly imply that the simulated track morphology is capable of describing the irradiated samples even for high fluences. Consequently, the dynamics leading to this morphology, namely recrystallisation (with and without

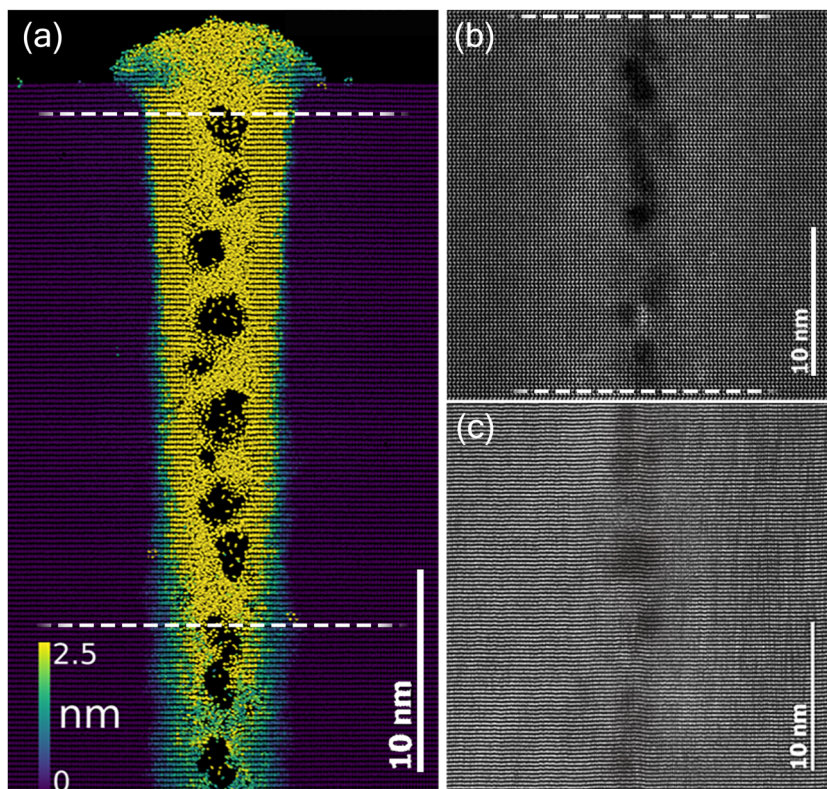


Fig. 4 Cross-sectional images of the final state of the track formed by a 185 MeV Au ion near the surface. **a** Simulated track with the colour scale representing the magnitude of displacement of the atoms from their initial positions. **b** Simulated transmission electron microscopy-high-angle annular dark-field image corresponding to the area delimited by the dashed lines in **(a)**. **c** Corresponding experimental cross-sectional image of a track near the surface of a sample irradiated with a fluence of $1 \times 10^{11} \text{ cm}^{-2}$.

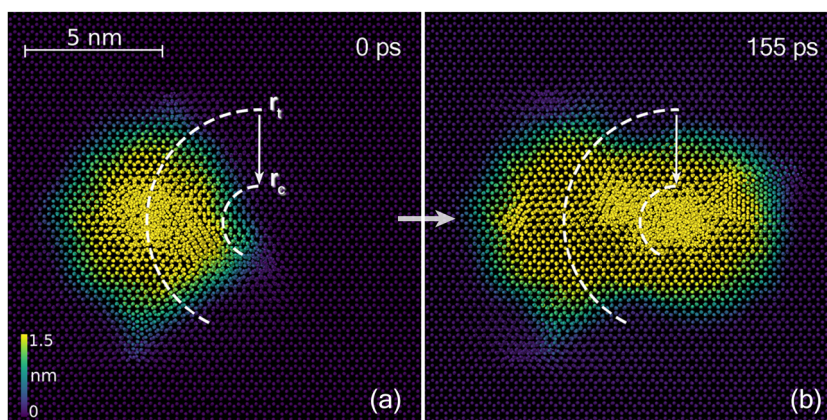


Fig. 5 Recrystallisation of the ion track when overlapped by a second ion for the case of the 185 MeV Au irradiation in the deeper regions. **a** Plan-view image of a track induced by a first impact. **b** Final stage of the cell after an impact overlap event. The concentric circles mark the position of the second impact with the inner and outer circles representing the amorphous and recrystallised cross-sections of the track, respectively.

overlapping) and sputtering, do occur when the SHIs impact the crystal.

Galactic cosmic radiation. To validate the established modelling scheme (including the thermodynamic parameters) also for lower SHI energies, closer to those found in GCR, we apply the same procedure to study GaN films irradiated with 70 and 45 MeV Xe ions ($\epsilon_e = 19.9$ and 14.9 keV/nm^{24} , respectively) with a fluence of $2 \times 10^{12} \text{ cm}^{-2}$.

The simulations demonstrate a track dynamics similar to that described above for the 185 MeV Au ion but with a considerably

smaller track radius. After 6 ps, r_t reaches its maximum value of 2.8 and 2.2 nm for the 70 and 45 MeV Xe ions, respectively, instead of the 4.4 nm obtained for the more energetic Au ions. The recrystallisation process in both Xe radiations recovers most of the initial damage and forms considerably fewer extended defects than the Au radiation. When the crystal reaches room temperature, the tracks present discontinuous cores consisting mostly of small amorphous pockets ($r_c < 1 \text{ nm}$) that get almost completely recrystallised when overlapped by another SHI impact. Although sputtering still occurs, the presence of voids is very superficial, with depths of 18 and 5 nm for 70 and 45 MeV

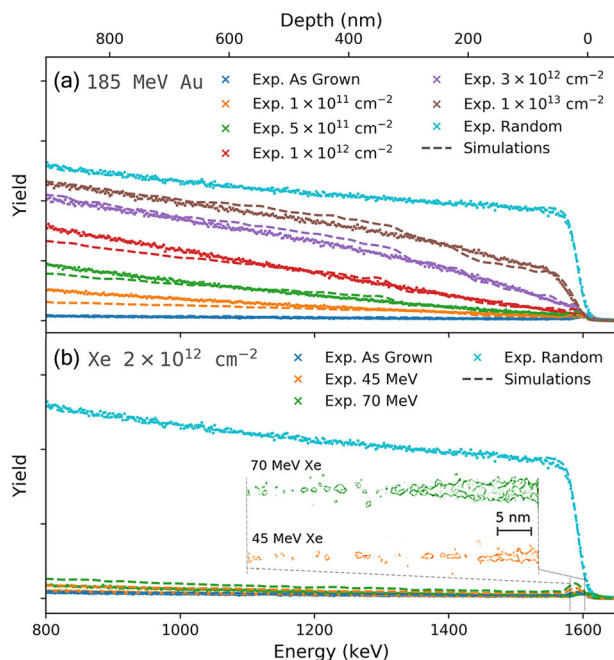


Fig. 6 Rutherford backscattering spectrometry/channelling data of irradiated samples. Aligned and random RBS/C spectra of the samples (symbols) and corresponding simulations (lines) for **a** 185 MeV Au, **b** 70 and 45 MeV Xe irradiations. The aligned spectra are obtained by aligning the probe beam along the [001] axis of the samples. The random spectra are collected from the as-grown sample by tilting it by 5° with respect to the probe beam direction and rotating the sample during the measurement. The inset shows the dislocation extraction algorithm output from the surface simulations for the Xe ions.

Xe, respectively. The DXA analysis, shown in Fig. 6b, evidences these conclusions.

We present the RBS/C results in Fig. 6b. Remarkably, the results reveal that both Xe SHIs induce nearly no damage in the crystal, even for a relatively high fluence of $2 \times 10^{12} \text{ cm}^{-2}$. The yields of the aligned spectra of the samples irradiated with 45 MeV Xe ions and as-grown samples are comparable within the experimental uncertainty. The RBSADEC simulations are in good agreement with the experiment. The slight overestimation of the yields is most likely related to the high defect mobility of point defects in GaN, shown to be mobile at 120 K³², leading to defect recovery at time scales not represented by the MD simulations.

Discussion

The excellent qualitative and quantitative agreement between the simulations, TEM, EELS and RBS/C results indicates that the employed model has a significant prediction power. The simulations unveil a strong recrystallisation effect that is responsible for recovering most of the initial melted region induced by the SHI. Interestingly, the effect can recover the damage produced by previous ion impacts, including the amorphous cores of the tracks. This dynamical recovery is of paramount relevance since it lowers the damage evolution with the irradiation fluence considerably, preventing the complete amorphisation of the crystal. Moreover, it is also responsible for the unusual resistance of GaN to strongly ionising radiation.

The model can be used to inspect a broad range of applications and predict the behaviour of GaN under extreme radiation conditions, including the formation of defects such as point and extended defects, amorphous cores, density gradients and voids. This eases the burden of going through complicated and

expensive experimental work that characterises this radiation regime. Considering space applications, the multiplicity of ion species and energies natural of this environment can further aggravate these studies. We note that the ϵ_e of the Fe component of the HZE radiation peaks at 14 keV/nm ^{8,9,24}, which is close to the one of the 45 MeV Xe ions studied here. Therefore, we anticipate that important device properties, such as rate of failure, dose thresholds, shielding design, among others, can be better estimated and understood. For instance, our results for the 185 MeV Au radiation are comparable with those reported³³ where GaN-based HEMTs were irradiated with 1540 MeV Bi ions ($\epsilon_e = 45.9 \text{ keV/nm}$). Considering the use of SHIs as a tool for material engineering³⁴, our model can give new insights into the influence of the radiation parameters on the planned design.

Methods

Experimental details

Materials. Commercial c-GaN thin films (Lumilog), 3- μm thick, grown by Metal Organic Chemical Vapour Deposition on Al_2O_3 substrates were used.

Radiations. The samples were irradiated with 185 MeV Au^{13+} ($\epsilon_e = 33 \text{ keV/nm}$ according to simulations done with the Monte Carlo code SRIM²⁴) ions at the Australian National University Heavy Ion Accelerator Facility with fluences of 10^{11} , 10^{12} and 10^{13} cm^{-2} at room temperature. Moreover, an energy study was performed using a 90 MeV Xe^{23+} beam at the Grand Accélérateur National d'Ions Lourds (GANIL). The beam energy was degraded to 70 and 45 MeV Xe ($\epsilon_e = 19.9$ and 14.9 keV/nm ²⁴, respectively) using Al foils of different thickness. The fluence for both energies was $2 \times 10^{12} \text{ cm}^{-2}$. All irradiation shown here were performed with a zero-angle incidence with respect to the surface normal. Note that ϵ_e is calculated using the SRIM code, which does not consider the charge state of the SHIs. Hence, their values may be smaller than the ones given above in the region very near the surface.

Transmission electron microscopy–high-angle annular dark-field (TEM-HAADF). High-resolution TEM and scanning TEM experiments were performed on a double corrected JEOL ARM 200F operating at 200 kV. In scanning TEM mode, this microscope provides a spatial resolution of 0.078 nm. STEM analyses were carried out using an HAADF detector at the inner and outer angles of 68 and 280 mrad to reduce diffraction contrast efficiently. The samples were prepared for plan-view and cross-sectional observations with the focused-ion-beam method using 30 keV Ga^+ ions in a Helios Nanolab 660 system (ThermoFisher). The ion energy was decreased to 2 keV in several steps to obtain the samples with thicknesses lower than 100 nm. Finally, the samples were cleaned with a plasma cleaner immediately before being measured.

Electron energy loss spectroscopy (EELS). EELS experiments were performed with a collection angle of 90 mrad. Elemental mapping was recorded with a dispersion of 1 eV/channel. HR-TEM/STEM micrographs and EELS data were acquired and processed under Gatan Digital Micrograph environment.

Rutherford backscattering spectrometry/channelling (RBS/C). The RBS/C measurements were performed at LATR (Laboratório de Aceleradores e Tecnologias de Radiação) IST using a Van de Graaff accelerator. A 2 MeV He^+ probe beam was used, and the backscattered particles were detected using a pin-diode detector at a backscattering angle of 165° . The aligned measurements were performed along the *c*-axis of the wurtzite crystals with the help of a two-axes goniometer. For the random spectra, to avoid channelling, the samples were tilted by 5° from the channelling direction and the azimuthal angle rotated during the measurement. Due to the similarities between the random spectra, only the spectrum from the as-grown sample is shown here. The presence of defects increases the backscattering yield in the aligned spectra. In the extreme case of complete amorphisation, the aligned spectrum would reach the random one, since the channelling effect becomes impossible. Therefore, comparing the two spectra allows for a quantification of the defect density in the crystals. The energy-depth scale is obtained considering the energy loss of the probe ions in the material.

Simulation details

Two-temperature model (TTM). Being a thermodynamic model, the TTM depends on the heat capacity and conductivity, *C* and *K*, respectively, of the lattice and electrons as well as on the electron-phonon coupling, *g*. For GaN, the parameters for the lattice have been measured^{35,36}. In contrast, the electronic parameters are yet unknown. In the context of the TTM, the conduction electrons are usually assumed to have a metal-like behaviour and *C_e* and *K_e* are considered constant (e.g.,^{18,19,22}) or have a linear dependence with the electronic temperature, *T_e*¹³. However, it has been shown that even for pure metals, this approximation can be misleading³⁷, and even more questionable for semiconductors as discussed for

SiC³⁸. Here we introduce a simple T_e dependence in C_e , K_e and g by applying the effective mass theory for semiconductors to a free electron gas in the GaN Γ -valley. As a consequence, the electron relaxation time τ_e (i.e., the time at which T_e is reduced to $1/e$) remains as the only free parameter of the model, here estimated to be 85 fs. A detailed discussion on the implementation of the TTM for GaN is presented in Supplementary Note 1.

The use of equilibrium thermodynamic quantities to describe a process far from equilibrium must be taken with some care. Yet, the excellent agreement between experimental and theoretical results presented here and previously for other semiconductors and insulators^{12,39,40} suggests that the simplicity and low computational costs offset the small deviations that may arise due to non-equilibrium physics. However, it is important to note that the TTM does not take into consideration the structural dynamics of the crystal hence hiding compelling phenomena such as phase transitions or defect dynamics. Thus, in this work, its validity is assumed only until 90% of the initial electronic energy has been transferred into the lattice (i.e., the first ~80 fs). We then transfer the energy profile of the lattice, resultant from the TTM, into a MD cell (see Supplementary Note 1B).

MD simulations (MD). The MD cells are relaxed until reaching room temperature (155 ps after the ion impact) using the Albe–Nord potential⁴¹ implemented in the PARCAS code⁴². Typically, SHIs have ranges longer than the thickness of our GaN films. Since for the SHIs under study, ϵ_e has a relatively slow decrease with depth²⁴, its value is considered constant. To account for surface effects in the interaction dynamics, we perform MD simulations for bulk and surface separately. In the former, periodic boundary conditions in all three directions are imposed while in the latter, the periodicity normal to the SHI trajectory is removed. In both cases, a Berendsen temperature control⁴³ is applied at the boundaries parallel to the SHI trajectory. In addition, in order to replicate a real size thin film in the surface simulations, yet keeping the computation cost reasonable, a fast thermostat is set at the bottom of the cell to prevent surface effects at this boundary. All simulations are done using $30 \times 30 \times 50 \text{ nm}^3$ cells. The visualisation of the simulations is done using the software OVITO⁴⁴.

Transmission electron microscopy–high-angle annular dark-field (TEM-HAADF) simulations. To better compare the TTM-MD simulated track with TEM-HAADF images, we note that this technique is highly sensitive to the atomic number of the atoms of the sample ($\propto Z^2$). Thus, we compute the average of Z^2 at each atom site, considering its neighbouring atoms within a cutoff radius of 1 nm. This value is then represented using a greyscale that is linearly adjusted to match the TEM-HAADF image contrast.

Electron energy loss spectroscopy (EELS) simulations. The density profile is obtained by determining the atomic density within vertical slices (each with a width of 0.5 Å and over the entire 30 nm depth of the MD cell) perpendicular to the plane of view (i.e., the experimental scan direction). By calculating the average over a window of multiple slices and plotting it at the centre of each slice, it is possible to introduce the experimental resolution and therefore compare the simulation with the EELS measurements. In Fig. 3c, we show the simulated densities obtained using average windows with a total width of 1.3 nm (orange line) and 6 nm (green line).

RBSADEC simulations. To create a realistic cell for RBS/C simulations using the TTM-MD results, we need to consider the effects of the fluence and the depth inhomogeneities. A given fluence can be described by the number of impacts in the cell, N , and the distance between them, D . Note that D is an essential parameter due to the observed distinction between direct and non-direct overlap effects in the final track morphologies. N is calculated according to Poisson statistics. Regarding D , we calculate it by simulating the random position of a large number of impacts (corresponding to the fluence) and computing the average distance between each impact and its nearest neighbour. Afterwards, we run TTM-MD simulations (bulk and surface) for each set of N and D parameters.

The depth inhomogeneities are introduced by combining the cells from the bulk and surface simulations. For the deeper regions, the entire bulk cell is repeated until a thickness of t_b . For the surface region, we slice the surface cell into thinner sub-cells and repeat each of these to obtain the desired thickness, t_s . The thickness of the final cell, $t_b + t_s$, is set to 1200 nm, the typical depth seen in RBS/C. As mentioned in the text, t_s assumes a distribution instead of a fixed value. This distribution is introduced by performing RBS/C simulations using n different t_s^i , with n depending on the fluence. The obtained spectra, $S(t_s^i)$, are then averaged to produce the total spectrum $S_{\text{total}} = \frac{1}{n} \sum_i S(t_s^i)$. For most fluences, besides using a minimum and maximum t_s^i (50 and 320 nm, respectively), we add a simulation using $t_s^i = 205 \text{ nm}$ to account for the fact that t_s assumes values tendentially closer to its maximum.

Except for the surface part, the same process is applied to study the samples irradiated with Xe ions (with a fluence of $2 \times 10^{12} \text{ cm}^{-2}$). Since the surface morphology is fully contained in the surface MD cell (see DXA in Fig. 6), we can simply append this cell to the bulk cells.

For further details on the implementation of the RBSADEC, please refer to Supplementary Note 2.

Data availability

Supplementary Movie 1 shows the evolution of the melted track formed after the impact of a 185 MeV Au ion from which the plan-view images shown in Fig. 1 are taken. Further material that supports the findings of this study is available from the corresponding author upon reasonable request.

Received: 30 July 2020; Accepted: 10 February 2021;

Published online: 12 March 2021

References

- Pengelly, R. S., Wood, S. M., Milligan, J. W., Sheppard, S. T. & Pribble, W. L. A review of GaN on SiC high electron-mobility power transistors and MMICs. *IEEE Trans. Microw. Theory Techn.* **60**, 1764–1783 (2012).
- Pearnton, S. J., Ren, F., Patrick, E., Law, M. E. & Polyakov, A. Y. Review—ionizing radiation damage effects on GaN devices. *ECS J. Solid State Sci. Technol.* **5**, Q35–Q60 (2016).
- Richard, Y. et al. In-flight experience and results of the PROBA-V low cost X-Band HDR-TM Transmitter. The 4S Symposium 20141–14 (2014).
- ESA. European Space Agency—key components of tree-counting biomass radar cleared for space. http://www.esa.int/our_activities/space_engineering_technology/key_components_of_treecounting_biomass_radar_cleared_for_space (2018).
- Ruterana, P., Lacroix, B. & Lorenz, K. A mechanism for damage formation in GaN during rare earth ion implantation at medium range energy and room temperature. *J. Appl. Phys.* **109**, 013506 (2011).
- Lorenz, K. et al. Implantation damage formation in a-, c- and m-plane GaN. *Acta Mater.* **123**, 177–187 (2017).
- Kucheyev, S. O., Williams, J. S. & Pearnton, S. J. Ion implantation into GaN. *Mater. Sci. Eng. R Rep.* **33**, 51–108 (2001).
- ESA. European Space Agency. www.spenvis.oma.be.
- Tylka, A. et al. CREME96: a revision of the cosmic ray effects on micro-electronics code. *IEEE Trans. Nucl. Sci.* **44**, 2150–2160 (1997).
- Hassler, D. M. et al. Mars' surface radiation environment measured with the Mars science laboratory's curiosity rover. *Science* **343**, 1244797 (2014).
- Galloway, K. F. et al. Failure estimates for SiC power MOSFETs in space electronics. *Aerospace* **5**, 67 (2018).
- Kluth, P. et al. Fine structure in swift heavy ion tracks in amorphous SiO₂. *Phys. Rev. Lett.* **101**, 175503 (2008).
- Ochedowski, O. et al. Graphitic nanostructures in silicon carbide surfaces created by swift heavy ion irradiation. *Nat. Commun.* **5**, 3913 (2014).
- Zhang, Y. et al. Ionization-induced annealing of pre-existing defects in silicon carbide. *Nat. Commun.* **6**, 8049 (2015).
- Debelle, A. et al. Combined experimental and computational study of the recrystallization process induced by electronic interactions of swift heavy ions with silicon carbide crystals. *Phys. Rev. B Condens. Matter Mater. Phys.* **86**, 100102(R) (2012).
- Backman, M. et al. Molecular dynamics simulations of swift heavy ion induced defect recovery in SiC. *Comput. Mater. Sci.* **67**, 261–265 (2013).
- Weber, W. J., Duffy, D. M., Thomé, L. & Zhang, Y. The role of electronic energy loss in ion beam modification of materials. *Curr. Opin. Solid State Mater. Sci.* **19**, 1–11 (2015).
- Lang, M., Devanathan, R., Toulemonde, M. & Trautmann, C. Advances in understanding of swift heavy-ion tracks in complex ceramics. *Curr. Opin. Solid State Mater. Sci.* **19**, 39–48 (2015).
- Sall, M. et al. Track formation in III-N semiconductors irradiated by swift heavy ions and fullerene and re-evaluation of the inelastic thermal spike model. *J. Mater. Sci.* **50**, 5214–5227 (2015).
- Kucheyev, S. O. et al. Lattice damage produced in GaN by swift heavy ions. *J. Appl. Phys.* **95**, 5360–5365 (2004).
- Gibbons, J. Ion implantation in semiconductors—Part II: damage production and annealing. *Proc. IEEE* **60**, 1062–1096 (1972).
- Toulemonde, M., Dufour, C., Meftah, A. & Paumier, E. Transient thermal processes in heavy ion irradiation of crystalline inorganic insulators. *Nucl. Instrum. Methods Phys. Res. B* **166**, 903–912 (2000).
- Vázquez, H. et al. Creating nanoporous graphene with swift heavy ions. *Carbon* **114**, 511–518 (2017).
- Ziegler, J. F., Biersack, J. P. & Littmark, U. *The Stopping and Range of Ion in Solids*. (Springer, Boston, MA, 1985).
- Utsumi, W. et al. Congruent melting of gallium nitride at 6 GPa and its application to single-crystal growth. *Nat. Mat.* **2**, 735–738 (2003).
- Stukowski, A., Bulatov, V. V. & Arsenlis, A. Automated identification and indexing of dislocations in crystal interfaces. *Model. Simul. Mater. Sci. Eng.* **20**, 085007 (2012).
- Cai, B. & Drabold, D. A. Properties of amorphous GaN from first-principles simulations. *Phys. Rev. B Condens. Matter Mater. Phys.* **84**, 075216 (2011).

28. Bogh, E. Defect studies in crystals by means of channeling. *Can. J. Phys.* **46**, 653–662 (1968).
29. Gärtner, K. Axial dechanneling in compound crystals with point defects and defect analysis by RBS. *Nucl. Instrum. Methods Phys. Res. B* **132**, 147–158 (1997).
30. Jozwik, P. et al. Monte Carlo simulations of ion channeling in crystals containing dislocations and randomly displaced atoms. *J. App. Phys.* **126**, 195107 (2019).
31. Zhang, S. et al. Simulation of Rutherford backscattering spectrometry from arbitrary atom structures. *Phys. Rev. E* **94**, 043319 (2016).
32. Lorenz, K. et al. Radiation damage formation and annealing in GaN and ZnO. *Oxide-based Materials and Devices II—Proceedings of SPIE* **7940**, 79400O (2011).
33. Hu, P. P. et al. Degradation in AlGaIn/GaN HEMTs irradiated with swift heavy ions: role of latent tracks. *Nucl. Instrum. Methods Phys. Res. B* **430**, 59–63 (2018).
34. Pérez-Mitta, G., Toimil-Molaes, M. E., Trautmann, C., Marmisollé, W. A. & Azzaroni, O. Molecular design of solid-state nanopores: fundamental concepts and applications. *Adv. Mater.* **31**, 1901483 (2019).
35. Shibata, H. et al. High thermal conductivity of gallium nitride (GaN) crystals grown by HVPE process. *Mater. Trans.* **48**, 2782–2786 (2007).
36. Jacob, K. T., Singh, S. & Waseda, Y. Refinement of thermodynamic data on GaN. *J. Mater. Res.* **22**, 3475–3483 (2007).
37. Lin, Z., Zhigilei, L. V. & Celli, V. Electron-phonon coupling and electron heat capacity of metals under conditions of strong electron-phonon nonequilibrium. *Phys. Rev. B Condens. Matter Mater. Phys.* **77**, 075133 (2008).
38. Khara, G. S., Murphy, S. T., Daraszewicz, S. L. & Duffy, D. M. The influence of the electronic specific heat on swift heavy ion irradiation simulations of silicon. *J. Phys. Condens. Matter* **28**, 395201 (2016).
39. Mota-Santiago, P. et al. Nanoscale density variations induced by high energy heavy ions in amorphous silicon nitride and silicon dioxide. *Nanotechnology* **29**, 144004 (2018).
40. Ridgway, M. C. et al. Tracks and voids in amorphous Ge induced by swift heavy-ion irradiation. *Phys. Rev. Lett.* **110**, 245502 (2013).
41. Nord, J., Albe, K., Erhart, P. & Nordlund, K. Modelling of compound semiconductors: analytical bond-order potential for gallium, nitrogen and gallium nitride. *J. Phys. Condens. Matter* **15**, 5649–5662 (2003).
42. Nordlund, K. et al. Defect production in collision cascades in elemental semiconductors and fcc metals. *Phys. Rev. B Condens. Matter Mater. Phys.* **57**, 7556–7570 (1998).
43. Berendsen, H. J., Postma, J. P., Van Gunsteren, W. F., Dinola, A. & Haak, J. R. Molecular dynamics with coupling to an external bath. *J. Chem. Phys.* **81**, 3684–3690 (1984).
44. Stukowski, A. Visualization and analysis of atomistic simulation data with OVITO—the Open Visualization Tool. *Model. Simul. Mater. Sci. Eng.* **18**, 015012 (2010).

Acknowledgements

Financial support by FCT, Portugal and FEDER is acknowledged (PTDC/CTM-CTM/28011/2017, LISBOA-01-0145-FEDER-028011, UID/05367/2020). M.C.S. thanks FCT Portugal for his PhD grant (SFRH/BD/111733/2015). J.-G.M. thanks ANR-10-LABX-09-

01 (LabEx EMC3) for his post-doctoral grant. This work was partially supported by the ANR funding ‘Investissements d’avenir’ ANR-11-EQPX-0020 (Equipex GENESIS), by the ‘Fonds Européen de Développement Régional’ and by the Région Basse-Normandie. P.K. acknowledges the Australian Research Council for financial support. Au irradiation was conducted at the ANU Heavy Ion Accelerator Facility (HIAF). Operations of the ANU HIAF is financially supported by the National Collaborative Research Infrastructure Strategy (NCRIS) HIA capability in Australia. We acknowledge the GANIL for the Xe beamtime available under the project CIMAP/IPAC2016/LB/P1110-M-S. We thank I. S. Roqan (KAUST) for the GaN samples.

Author contributions

M.C.S. and K.L. conceived the project. M.C.S. applied the TTM to GaN and performed all the TTM-MD simulations with contributions from H.V., F.D. and K.N. The experimental TEM images were obtained by J.-G.M. and I.M. The SHI irradiations were performed by I.M., C.G., P.M.-S. and P.K. The RBS/C measurements were obtained by M.C.S. with the supervision of E.A. and K.L. M.C.S. performed the RBS/C simulations with contributions from S.Z. The manuscript was written by M.C.S. with input from all co-authors. K.L. supervised the project. All authors discussed the results and approved the manuscript.

Competing interests

The authors declare no competing interests.

Additional information

Supplementary information The online version contains supplementary material available at <https://doi.org/10.1038/s42005-021-00550-2>.

Correspondence and requests for materials should be addressed to M.C.S.

Reprints and permission information is available at <http://www.nature.com/reprints>

Publisher’s note Springer Nature remains neutral with regard to jurisdictional claims in published maps and institutional affiliations.



Open Access This article is licensed under a Creative Commons Attribution 4.0 International License, which permits use, sharing, adaptation, distribution and reproduction in any medium or format, as long as you give appropriate credit to the original author(s) and the source, provide a link to the Creative Commons license, and indicate if changes were made. The images or other third party material in this article are included in the article’s Creative Commons license, unless indicated otherwise in a credit line to the material. If material is not included in the article’s Creative Commons license and your intended use is not permitted by statutory regulation or exceeds the permitted use, you will need to obtain permission directly from the copyright holder. To view a copy of this license, visit <http://creativecommons.org/licenses/by/4.0/>.

© The Author(s) 2021